


## RESEARCH ARTICLE

# Single Extracellular Vesicle Nanoscopy

Andras Saftics<sup>1</sup>  | Sarah Abuelreich<sup>1</sup> | Eugenia Romano<sup>1</sup> | Ima Ghaeli<sup>1</sup> | Nan Jiang<sup>1</sup> |  
 Michail Spanos<sup>2</sup> | Kathleen M. Lennon<sup>1</sup> | Gagandeep Singh<sup>3</sup> | Saumya Das<sup>2</sup> |  
 Kendall Van Keuren-Jensen<sup>4</sup> | Tijana Jovanovic-Talisan<sup>1</sup>

<sup>1</sup>Department of Cancer Biology and Molecular Medicine, Beckman Research Institute, City of Hope Comprehensive Cancer Center, Duarte, California, USA

<sup>2</sup>Cardiology Division and Corrigan Minehan Heart Center, Massachusetts General Hospital, Harvard Medical School, Boston, Massachusetts, USA

<sup>3</sup>Department of Surgery, City of Hope Comprehensive Cancer Center, Duarte, California, USA

<sup>4</sup>Neurogenomics Division, Translational Genomics Research Institute, Phoenix, Arizona, USA

## Correspondence

Tijana Jovanovic-Talisan, Department of Cancer Biology and Molecular Medicine, Beckman Research Institute, City of Hope Comprehensive Cancer Center, Duarte, CA 91010, USA.  
 Email: [ttalisan@coh.org](mailto:ttalisan@coh.org)

## Funding information

Dancing with Chicago Celebrities; Irell and Manella Graduate School of Biological Sciences at City of Hope; Circle 1500; Dorrance Family Research Fund; Bruce & Lyn Everette; Southwest Food Industries Circle; Board of Governors of the City of Hope; National Institutes of Health, Grant/Award Numbers: P30CA033572, UG3/UH3 TR002878

## Abstract

Extracellular vesicles (EVs) and their cargo constitute novel biomarkers. EV subpopulations have been defined not only by abundant tetraspanins (e.g., CD9, CD63 and CD81) but also by specific markers derived from their source cells. However, it remains a challenge to robustly isolate and characterize EV subpopulations. Here, we combined affinity isolation with super-resolution imaging to comprehensively assess EV subpopulations from human plasma. Our Single Extracellular Vesicle Nanoscopy (SEVEN) assay successfully quantified the number of affinity-isolated EVs, their size, shape, molecular tetraspanin content, and heterogeneity. The number of detected tetraspanin-enriched EVs positively correlated with sample dilution in a 64-fold range (for SEC-enriched plasma) and a 50-fold range (for crude plasma). Importantly, SEVEN robustly detected EVs from as little as  $\sim 0.1 \mu\text{L}$  of crude plasma. We further characterized the size, shape and molecular tetraspanin content (with corresponding heterogeneities) for CD9-, CD63- and CD81-enriched EV subpopulations. Finally, we assessed EVs from the plasma of four pancreatic ductal adenocarcinoma patients with resectable disease. Compared to healthy plasma, CD9-enriched EVs from patients were smaller while IGFIR-enriched EVs from patients were larger, rounder and contained more tetraspanin molecules, suggestive of a unique pancreatic cancer-enriched EV subpopulation. This study provides the method validation and demonstrates that SEVEN could be advanced into a platform for characterizing both disease-associated and organ-associated EV subpopulations.

## KEYWORDS

extracellular vesicles (EVs), nanoscopy, pancreatic ductal adenocarcinoma (PDAC), quantitative single molecule localization microscopy (qSMLM), SEVEN, single EV analysis

## 1 | INTRODUCTION

Every cell releases membrane-encapsulated particles known as extracellular vesicles (EVs) that may mediate intercellular communication through their cargo: nucleic acids, metabolites, lipids and proteins (Yáñez-Mó et al., 2015). These cargoes, which are derived from the source cells of EVs (Colombo et al., 2014; Kowal et al., 2016; Ratajczak et al., 2006), may reflect tissue or disease-specific phenotypes. For example, when cells undergo phenotypic changes, EVs reflect alterations in homeostasis and can rapidly report on the disease status (Bei et al., 2017; Cherbonneau et al., 2022). EVs thus have become enticing sources of biomarkers for a wide array of diseases. However, a primary source for sampling patient EVs—easily accessed biofluids—contains a complex mixture of EVs released from cells across the entire body. Not only do these EVs encompass diverse biophysical characteristics,

This is an open access article under the terms of the [Creative Commons Attribution-NonCommercial License](https://creativecommons.org/licenses/by-nc/4.0/), which permits use, distribution and reproduction in any medium, provided the original work is properly cited and is not used for commercial purposes.

© 2023 The Authors. *Journal of Extracellular Vesicles* published by Wiley Periodicals, LLC on behalf of the International Society for Extracellular Vesicles.

but also, they comprise a broad range of sizes ( $\sim 30$  nm– $10$   $\mu$ m) (Di Vizio et al., 2009; Doyle & Wang, 2019; Willms et al., 2018). Moreover, biofluids harbour merely a small fraction of EVs derived from cells that underwent phenotypic changes. The ability to rigorously isolate and characterize EV subpopulations with high sensitivity remains an urgent, unmet need for advancing them as robust sources of biomarkers.

The heterogeneity of EVs within patient samples, when juxtaposed with the need to study specific EV subpopulations, has prompted a broad range of approaches for their isolation. Conventional methods to isolate EVs can group them into fractions based on their size, charge and/or density (Doyle & Wang, 2019; Willms et al., 2018; Yáñez-Mó et al., 2015). Further selectivity can be achieved by targeting specific biomolecules located on EV membranes. For example, most EVs contain common tetraspanins such as CD9, CD63 and CD81; selective antibodies against these tetraspanins can be used to affinity isolate a wide range of EVs. Moreover, EVs carry specific membrane proteins derived from their source cells (Kowal et al., 2016). These proteins can be enriched in certain tissue types or diseases and used as handles to select for specific EV subpopulations. Selectivity is especially relevant for diagnostic applications; assessing cargo from tissue-specific EVs may improve their capacity to serve as biomarkers.

To provide an efficient strategy for assessing specific EV subpopulations, here we developed a new approach called Single Extracellular Vesicle Nanoscopy (SEVEN). SEVEN combines affinity isolation with a super-resolution fluorescence microscopy method called quantitative single molecule localization microscopy (qSMLM). qSMLM can achieve single-molecule sensitivity, nanoscale resolution and robust molecular counting (Golfetto et al., 2018; Khater et al., 2020; Lelek et al., 2021). It has been used to define EV size (Gebara et al., 2022; Lennon et al., 2019, 2022; Mondal et al., 2019; Nizamudeen et al., 2018; Sharma et al., 2020; Zong et al., 2018) and localize EV cargo (Lennon et al., 2019, 2022; Maire et al., 2021; Oleksiuk et al., 2015; Silva et al., 2021). Importantly, compared to other techniques for single EV characterization, qSMLM has superior sensitivity (Silva et al., 2021). This property is essential for detecting low-abundant EV subpopulations (e.g., those derived from early-stage tumours). Here we applied SEVEN to assess EVs isolated from the plasma of healthy subjects and patients with resectable pancreatic ductal adenocarcinoma (PDAC).

PDAC has increasing incidence and it is projected to become the second leading cause of cancer-related death by 2030 (Rahib et al., 2014). Because symptoms of PDAC are often nonspecific (Li et al., 2004; Von Hoff et al., 2013), only 10%–20% of patients present with resectable disease (PDAC resection is the only potentially curative treatment option). Current diagnostic tests do not improve long-term survival (Al-Sukhni et al., 2012; Kim et al., 2011). To improve patient outcomes, advances in treatment (Conroy et al., 2011; Von Hoff et al., 2013) need to be accompanied by new diagnostic approaches that have high sensitivity to detect early-stage tumours. Compared to other particles secreted from cancer cells (Ferguson et al., 2022), EVs have three main advantages: (1) they are secreted in high amounts (King et al., 2012; Lee et al., 2011); (2) the release of exosomes and microvesicles does not depend on cell death; (3) a recent meta-data study suggests that among liquid biopsy strategies, EVs have the highest specificity and sensitivity for PDAC detection (Zhu et al., 2020). Since PDAC-associated EVs are present in very low amounts in early disease stages ( $\sim 0.01\%$  of EVs may have disease markers) (Ferguson, Yang, & Weissleder, 2022; Ferguson, Yang, Zelga et al., 2022), new sensitive single EV assays that can detect PDAC-associated EVs from plasma are needed. Previously, we evaluated PDAC-associated EVs in advanced PDAC (Lennon et al., 2019). In a pilot study, here we used our sensitive SEVEN assay to assess EVs from four PDAC patients with the resectable disease and detected a pancreatic cancer-enriched EV subpopulation.

## 2 | MATERIALS AND METHODS

### 2.1 | Affinity reagents

The following antibodies (Abs) were used in the experiments of this study: anti-CD9 (BioLegend, Cat# 312102; San Diego, CA, USA), anti-CD63 (Novus Biologicals, Cat# NBP2-42225; Centennial, CO, USA), anti-CD81 (BioLegend, Cat# 349502), anti-IGF1R (ganitumab, a kind gift from Dr. J.C. Williams), anti-cytochrome C (BD Biosciences, Cat# 556432; Franklin Lakes, NJ, USA), anti-syntenin (Abcam, Cat# ab19903; Waltham, MA, USA) and anti-ApoA1 (Abcam, Cat# ab52945) Abs, as well as goat anti-rabbit (anti-rabbit IgG; Invitrogen, Cat# A16112; Waltham, MA, USA), IRDye 800CW goat anti-mouse (Li-Cor Biotechnology, Cat# 926–32210; Lincoln, NE, USA) and IRDye 680RD goat anti-rabbit (Li-Cor Biotechnology, Cat# 926–68071) secondary Abs. For ExoView experiments, fluorescently labelled anti-CD9-CF488A, anti-CD63-CF647 and anti-CD81-CF555 Abs from the manufacturer's kit were used (details below). Human lactadherin (MFG-E8), aa Leu24-Cys387 (contains both C1 and C2 domains) was purchased from Novus Biologicals (Cat# 2767-MF-050).

### 2.2 | Antibody conjugation with fluorophore

Anti-CD9, anti-CD63 and anti-CD81 Abs were conjugated with Alexa Fluor 647 N-hydroxysuccinimide (NHS) ester dye (AF647; Invitrogen, Cat# A20006) using previously reported protocol (Tobin et al., 2018). The degree of labelling was assessed by spectrophotometry using a NanoDrop 1000 instrument (Thermo Fisher Scientific). Typical degree of labelling was 1.0–1.5.

## 2.3 | Human plasma samples and patient cohort

Two types of human plasma samples were used in this study. The pooled human plasma was used as healthy control. Pooled human plasma (blood derived) was obtained from Innovative Research (Cat# IPLAWBK2E50ML, LOT# 34553; Novi, MI, USA). According to the protocol of Innovative Research, whole blood was collected from donors in an FDA-approved collection centre by the manufacturer. The blood was collected in K2 ethylenediaminetetraacetic acid (EDTA) containing dry blood collection bag, and it was spun at  $5000 \times g$  for 15 min in a refrigerated centrifuge. Plasma was isolated with a plasma extractor, frozen and shipped on dry ice. Upon receipt, the plasma was stored at  $-80^{\circ}\text{C}$ . The plasma from four PDAC patients (P1-P4) included in this study was collected under the Institutional Review Board (IRB) number 06129 (City of Hope Comprehensive Cancer Center) after informed consent was obtained from each subject. Blood from PDAC patients was collected in EDTA-containing lavender top blood collection tubes and was kept on ice until processed (typically within 1 h or less). The blood was transferred into a 15-mL conical tube and centrifuged at  $1200 \times g$  for 15 min at room temperature (RT). The plasma fraction was carefully transferred to a 15-mL conical tube and aliquoted into cryovials. The vials were immediately frozen and stored at  $-80^{\circ}\text{C}$ . The experimental team involved in this study was blinded to patient characteristics and was unblinded after all data collection and analysis were completed.

## 2.4 | Size exclusion chromatography (SEC) enrichment of EVs from plasma

EVs from pooled human plasma or PDAC patient plasma were enriched using Izon qEVoriginal Legacy 70 nm size exclusion chromatography (SEC) columns (Izon Science, Cat# SP1; Portland, OR, USA). Following column equilibration with phosphate-buffered saline (PBS), 400  $\mu\text{L}$  of plasma sample was loaded onto the column and  $13 \times 500 \mu\text{L}$  fractions (F) were collected (F1-F13) following the collection of the 3 mL void volume (VV). For further experiments, combined fractions F1-F5 were used.

## 2.5 | Negative staining transmission electron microscopy (TEM)

A 4  $\mu\text{L}$  of undiluted EV sample (SEC-enriched EVs from human pooled plasma and PDAC patient plasma) or 1:2 diluted recombinant EV reference material, rEVs (Millipore Sigma, Cat# SAE0193-1VL; Burlington, MA, USA) (Geurickx et al., 2019) was adsorbed onto glow discharged, carbon-coated 200 mesh electron microscopy grids for 5 min. The grids were then sequentially washed in deionized (DI) water three times for 30 s and were contrasted with 1% (w/v) uranyl acetate solution three times for 10 s. Transmission electron microscopy (TEM) images were acquired on an FEI Tecnai 12 transmission electron microscope (Thermo Fisher Scientific) at an acceleration voltage of 120 kV using LaB<sub>6</sub> filament. The images were captured with a Gatan 2 k  $\times$  2 k CCD camera (Gatan; Pleasanton, CA, USA). The  $4 \times 4 \mu\text{m}$  8-bit TEM images were converted into 16-bit images in ImageJ (National Institutes of Health, version 1.53t) and analysed using the TEM ExosomeAnalyzer software (version Aug 13, 2018) (Kotrbová et al., 2019), where individual EVs were outlined using the manual editing tool. The diameter and roundness of detected EVs were determined by the automatic analysis module, and EVs within the size range of 30–400 nm were considered. Samples from three independent repeats were analysed (in total 928 EVs were detected).

## 2.6 | Nanoparticle tracking analysis (NTA)

The EV concentration and size distribution of rEVs and SEC-enriched pooled human plasma samples were determined by nanoparticle tracking analysis (NTA) using an NS300 Nanosight instrument (Malvern Panalytical; Malvern, UK). The samples were injected into the sample chamber with a sterile syringe until the liquid reached the tip of the nozzle. All measurements were performed at RT. The samples for SEC-enriched pooled human plasma EVs were diluted 1:10 in 1 mL PBS, the samples for rEVs were diluted 1:200 in 1 mL PBS. Using default settings, three measurements were completed, each including a 60-s movie captured at 30 frames per second with manual shutter and gain adjustments. For statistical analysis of the NTA-determined size in Figure 1, only rEVs detected in the 30–400 nm size range were considered.

## 2.7 | Microfluidic resistive pulse sensing (MRPS)

Microfluidic resistive pulse sensing (MRPS) measurements were performed using a Spectradyn nCS1 with hardware version 2.5.0.325 (Spectradyn; Signal Hill CA, USA). The microfluidic system was primed with a solution of 0.1% (v/v) Tween-20 in PBS (PBS-T 0.1%). Instrument parameters were automatically determined by the device, including pressure at each cartridge

port and voltage at each bias electrode. We filtered our diluent with syringe filters of 0.02  $\mu\text{m}$  (Whatman® Anotop® 10) to avoid false-positive counts. Particle size distributions were determined using TS-400 cartridges (65 to 400 nm). Samples were diluted 1:100 in PBS-T 0.1%. For each measurement, 7  $\mu\text{L}$  of diluted sample was applied to the cartridge. All experiments consisted of continuous acquisitions until the standard error reached <2%, and experiments were repeated in triplicate. Upon completion of a measurement, the data were combined, and the nCSI Data Viewer was used to apply peak filters and background subtraction as directed by the manufacturer (version 2.5.0.325).

## 2.8 | Dot blots

We ran standard antibody dot blots and protein stain dot blots to assess the EV marker content and purity of the SEC-enriched pooled human plasma samples. The antibody dot blots on SEC-enriched pooled human plasma were performed according to the standard protocol of Li-Cor Biotechnology as reported previously (Lennon et al., 2022). The following primary antibodies were used: anti-CD9 at 1:500, anti-CD63 at 1:500, anti-CD81 at 1:500, anti-syntenin at 1:1000, anti-cytochrome C at 1:1000 and anti-ApoA1 at 1:1000 dilution. All the prepared blots were imaged using an Odyssey DLx system (Li-Cor Biotechnology). Protein stain dot blots were performed using SYPRO Ruby Protein Blot Stain (Thermo Fisher Scientific, Cat# S11791) according to the manufacturer's protocol.

## 2.9 | SEVEN assay

**Coverslip functionalization and Ab immobilization.** 25-mm diameter #1.5H glass coverslips (Thermo Fischer Scientific, Cat# NC9560650; Waltham, MA, USA) were cleaned as previously described (Golfetto et al., 2018; Tobin et al., 2018) and coated with MCP4 solution (Lucidant Polymers, Cat# MCP4-KIT; Sunnyvale, CA, USA). A 0.5  $\mu\text{L}$  of affinity reagent solution containing 1% glycerol was pipetted on the centre of each coverslip. Anti-IGF1R Ab was spotted at 1 mg/mL; a mixture of anti-CD9, anti-CD63, anti-CD81 Abs (anti-TSPAN Abs) was spotted at a final concentration of 0.17 mg/mL per Ab; lactadherin was spotted at 0.5 mg/mL, and all other Abs (anti-CD9, anti-CD63, anti-CD81, anti-rabbit IgG and anti-cytochrome C) were spotted at 0.5 mg/mL. Immediately after spotting, each coverslip was incubated for 4 h at RT in a humidity-controlled dish. Following incubation, the surfaces were washed and incubated in 1 mL Block-On blocking solution (Lucidant Polymers, Cat# 2X-BLK1) on an orbital shaker for 30 min at RT to cap unreacted sites. The coverslips were washed with a blocking buffer (BB) consisting of 2% (w/v) BSA and 0.025% (v/v) Tween-20 in PBS (PBS-T) followed by 0.025% (v/v) PBS-T.

**EV capture and staining.** EV samples were incubated onto coverslips overnight at RT on a rocking shaker and thoroughly washed with 0.025% (v/v) Tween-20 in PBS. EVs were stained with anti-TSPAN Abs-AF647 fluorescent probe solution (10 nM anti-CD9 Ab-AF647, 10 nM anti-CD63 Ab-AF647 and 10 nM anti-CD81 Ab-AF647 in 2% (w/v) BSA and 0.025% (v/v) Tween-20 in PBS). After washing, samples were fixed with 4% (w/v) paraformaldehyde (Electron Microscopy Sciences, Cat# 157-8; Hatfield, PA, USA) and 0.2% (w/v) glutaraldehyde (Electron Microscopy Sciences, Cat# 16019), quenched with 25 mM glycine in PBS, and rinsed with PBS, see Supplemental Methods for details. For two-colour imaging, available cysteines on EV membranes of SEC-enriched EVs from pooled human plasma were first labelled as described before (Lennon et al., 2022) using 10 nmol of CF568-maleimide (Thermo Fisher Scientific, Cat# 50-196-4845). Following the removal of excess dye with qEVsingle Legacy 70 nm SEC column (Izon Science, Cat# SP2), 150  $\mu\text{L}$  of isolated EVs in 0.025% (v/v) PBS-T were processed as described above.

**Imaging and analysis.** In SMLM, tetraspanins were detected with AF647-labelled anti-TSPAN Abs. Before they photobleach, these fluorescent reporters alternate between dark and fluorescent states (turn 'off' and 'on') (Annibale et al., 2011; Lee et al., 2012), allowing the detection of a subset of non-overlapping localizations in each frame. 25,000 frames are combined to produce a localization map. These maps are analysed (using Voronoi tessellation, see below) to detect EVs. To enable proper molecular counting, we determined photophysical properties of the fluorescent probes. In particular, we quantified the average number of localizations per individual fluorescent probe and maximum dark time using surface assay for molecular isolation (SAMI) (Golfetto et al., 2018). Here, the MCP4-coated surfaces were incubated with a mixture of 1 nM anti-CD9 Ab-AF647, 1 nM anti-CD63 Ab-AF647 and 1 nM anti-CD81 Ab-AF647 for 2 h. The surfaces were then washed and blocked (Coverslip Functionalization section). After PBS wash, surfaces were imaged. Analysis was done as previously described (Golfetto et al., 2018). We divide the number of detected localizations by the average number of localizations for a single fluorescent reporter (as determined by SAMI) to obtain the detected number of molecules.

The prepared surfaces were loaded into Attofluor cell chambers (Thermo Fisher Scientific, Cat# A7816) and were imaged by direct stochastic optical reconstruction microscopy (dSTORM). The surfaces were imaged in dSTORM imaging buffer (Dempsey et al., 2011). The images were acquired using a 3D N-STORM super-resolution microscope (Nikon Instruments; Melville, NY, USA) equipped with previously described components (Lennon et al., 2022). The 640 nm laser power used for excitation was 119.5 mW recorded out of the optical fibre. For each image, 25,000 frames were acquired at 10 ms exposure time on a region of



interest (ROI) of  $41 \times 41 \mu\text{m}$  ( $256 \times 256$  pixel). For two-colour imaging, sequential 640 and 561 nm acquisitions were collected as previously reported (Lennon et al., 2022) (25,000 frames and 10 ms exposure time in each channel, using 119.5 mW power in the 640 nm channel and 108.1 mW power in the 561 nm channel). The image acquisition was performed using the NIS-Elements software (Nikon Instruments, version 5.21.01 and 5.41.0) and peak localization was performed using the N-STORM Offline Analysis Module of the NIS-Elements software (version 5.21.01). The raw SMLM images were analysed in MATLAB (version R2022a; MathWorks; Natick, MA, USA) using custom code (Andronov et al., 2016; Lennon et al., 2019, 2022) (see details used for Voronoi tessellation in Supplemental Methods). Localization precision was estimated using the coordinate-based localization precision estimator (CBLPE) (Endesfelder et al., 2014) program in Python (version 2.7.18; Python Software Foundation; Wilmington, DE, USA) and Nikon's NIS-Elements software. Total internal reflection fluorescence (TIRF) imaging was performed with 488 nm laser with an exposure time of 30 ms and 1.6 mW excitation power recorded out of the optical fibre.

The characterization and analysis of rEVs by Extracellular Vesicle Spatial Clustering of Applications with Noise (EVSCAN) was performed in batches across multiple datasets using the Nanometrix software (version 1.0.4.61) developed by Nanometrix Ltd, Oxford, UK (<https://nanometrix.bio>). A search radius of 40 nm (distance to search for neighbouring points around each point) with 20 minimum points (number of neighbouring points including itself to define the current point as part of a dense cluster or not) and an EV factor of 0.1 (threshold value to include a localization as part of an EV cluster based on the cluster's localization density profile) were used for the analysis. The EVSCAN algorithm, developed by Nanometrix, is a variation of the density-based spatial clustering of applications (DBSCAN) algorithm designed to improve the clustering quality for EV localization data, by profiling each cluster for its density and removing low-density points within each cluster. Clusters with a minimum and maximum localization of 55 and 2800 and a minimum and maximum diameter of 30 and 400 nm, respectively, were identified as EVs. Two-colour (640 and 561 nm channel) data were aligned in Nanometrix software using the Uniform Dual Channel Alignment tool (the program iteratively finds colocalized EV clusters, measures the average distance and direction of overlapping cluster centroids, and adjusts one channel accordingly until the results converge), and the aligned data were analysed in Nanometrix using a search radius of 10 nm with 20 minimum points. Double-positive EVs were defined as two overlapping clusters of localizations from different channels, with a minimum and maximum number of localizations of 55 and 2800 detected in the 640 nm channel as well as minimum number of localizations of 55 per EV detected in the 561 nm channel. In both channels, clusters detected within a diameter range of 30–400 nm were considered as EVs. EV centroids in both the 640 and 561 nm channels were identified and the Euclidean distance between these centroids was subsequently calculated.

## 2.10 | EV characterization by the ExoView system

The size distribution and tetraspanin content of 1:200 diluted crude pooled human plasma and PDAC patient plasma samples ( $50 \mu\text{L}$ ) were analysed using an ExoView R100 system (NanoView Biosciences; using the ExoView Scanner 3.1.4 software), and either ExoView Human Tetraspanin Plasma Kit (NanoView Biosciences, Cat# EV-TETRA-P) or Leprechaun Exosome Human Plasma Kit (Unchained Labs, Cat# 251-1045; Pleasanton, CA, USA) were used by following the manufacturer's standard protocol. The chips were scanned in ExoView R100 both in the interferometric microscopy (IM) and in the fluorescence channels (with excitation wavelengths of 480, 555 and 640 nm). The collected data were analysed using the ExoView Analyzer 3.2 software (NanoView Biosciences). The EV counts per spot data were normalized to a spot size of  $150 \mu\text{m}$  diameter due to size differences between spots.

## 2.11 | Statistical information and graphics

Mean, standard error of the mean (SEM) and coefficient of variation (CV) values were determined using GraphPad Prism (version 9.5.1; GraphPad; San Diego, CA, USA), Excel (version 2209; Microsoft; Redmond, WA, USA) and MATLAB software. Statistical significance was determined using two-tailed two-sample Student's *t*-test with unequal variance. Significance levels were determined based on the resulting *p*-values and indicated as  $*p \leq 0.05$ ,  $**p \leq 0.01$ ,  $***p \leq 0.001$ . Due to the lognormal characteristic of the distribution of EV diameter, molecular tetraspanin content per EV (TSPAN/EV), and circularity, we applied a logarithmic transformation on each data set to approach normal distribution. *p*-values are provided in Supplemental Tables.

The graphs were generated in GraphPad Prism and MATLAB. Colorization of images of dot blots (Figure 2a) was performed in GIMP (2.10; unmodified versions are provided in Figure S3). All figures were finalized in Adobe Illustrator 2022 (version 26.5.3; Adobe; San Jose, CA, USA).

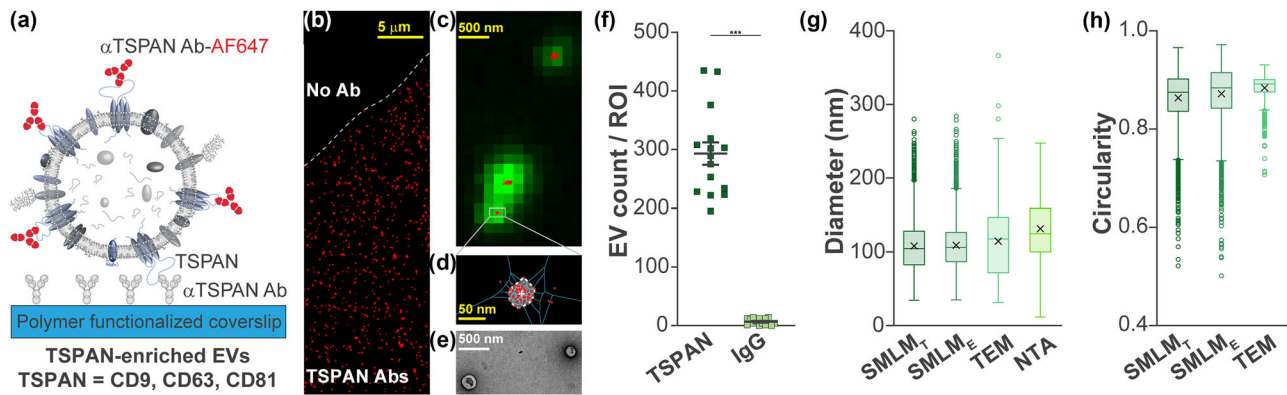


**FIGURE 1** Validation of EV size and shape measurements using SEVEN. (a) Scheme of an affinity isolated and fluorescently labelled EV. Anti-TSPAN Abs (mixture of unlabelled anti-CD9, anti-CD63 and anti-CD81 Abs) were covalently immobilized on the polymer-coated glass coverslip surface. After affinity capture, EVs were stained using a mixture of fluorescently labelled anti-TSPAN Abs. (b) Raw SMLM image of TSPAN-enriched EVs in red. (c) TSPAN-enriched EVs are imaged in SMLM (red, signal from fluorescent anti-TSPAN Abs) and TIRF (green, signal from GFP). (d) Tessellation polygons (blue lines) are outlining SMLM localization (red dots); EV is outlined in white dashed line using the Voronoi tessellation algorithm described in **Methods**. (e) TEM image of EVs. (f) Number of detected EVs per ROI for spot coated with either a mixture of anti-TSPAN Abs or anti-rabbit IgG control. (g) EV diameter detected with SMLM imaging and tessellation analysis (SMLM<sub>T</sub>); SMLM imaging and EVSCAN analysis (SMLM<sub>E</sub>); TEM and segmentation analysis; and NTA. (h) EV circularity detected with SMLM<sub>T</sub>, SMLM<sub>E</sub> and TEM. Box plots indicate interquartile range (box), median (centre line), mean (cross); the hollow dots (for TEM and SMLM) indicate EVs detected beyond 1.5-times the interquartile range (marked by the Whisker lines under and over the box). Error bars, SEM; \*\*\* indicates  $p < 0.001$ . Numerical values and  $p$ -values are provided in Tables S1 and S2.

### 3 | RESULTS

To comprehensively assess individual EVs, we developed Single Extracellular Vesicle Nanoscopy (SEVEN) assay that combines affinity isolation of EVs with qSMLM. To optimize and validate our approach, we employed commercially available recombinant EV reference material (rEVs) (Geurickx et al., 2019). In addition to common luminal and membrane-associated EV markers (including tetraspanins CD9, CD63 and CD81), a fraction of these EVs express gag polyprotein fused to enhanced green fluorescent protein (eGFP) (Geurickx et al., 2019). We first used SEVEN to assess tetraspanin-enriched rEVs.

Our protocol consists of seven main steps (details are provided in **Methods**). (1) Because tetraspanins CD9, CD63 and CD81 are typically abundant on EV surfaces, we used a mixture of Alexa Fluor 647 (AF647)-labelled antibodies (Abs) against these tetraspanins as fluorescent probes for EV staining. To enable efficient molecular counting (Golfetto et al., 2018), we characterized the photophysical properties of these fluorescent probes (see also **Methods**, Imaging and Analysis). In Figure S1, we show the average number of localizations per individual fluorescent probe and maximum dark time for AF647-labelled Abs against CD9, CD63 and CD81 (we refer to the mixture of these three Abs as anti-TSPAN Abs). (2) Coverslips were coated with a polymer that has dense NHS groups. Importantly, this polymer had a minimal background in SMLM and provided an excellent non-fouling surface when capped using blocking solution. (3) Affinity reagents (for rEVs we used unlabelled anti-TSPAN Abs) were covalently attached to polymer-coated coverslips via NHS chemistry; unreacted NHS groups were capped with blocking solution. (4) EVs were affinity captured onto coverslips. (5) Affinity-captured EVs were stained with AF647-labelled anti-TSPAN Abs (scheme in Figure 1a). (6) EVs were imaged using 2D SMLM. Figure 1b shows a raw SMLM image of rEVs with a clear border (dashed line) between the spot coated with anti-TSPAN Abs and passivated (non-fouling) coverslip surface. The zoomed in image (Figure 1c) shows an excellent overlap between SMLM signal in red (AF647-labelled anti-TSPAN Abs that stained rEVs) and total internal reflection fluorescence (TIRF) microscopy signal in green (eGFP within rEVs). We obtained an excellent signal-to-noise ratio that enables clear visualization of EVs. (7) Data was analysed using Voronoi tessellation-based algorithm (an example of tessellation analysis for an EV is shown in Figure 1d). Details of data analysis are provided in the **Methods** section. The outline of EV (dashed white line in Figure 1d), indicates a largely circular structure. This is expected from published transmission electron microscopy (TEM) images of rEVs (Geurickx et al., 2019) and our TEM images (Figure 1e).

We evaluated the number of rEVs (the same lot # of rEVs used for TEM) isolated either on anti-TSPAN Abs-coated spot or control anti-rabbit IgG-coated spot. From 0.33 μL of rEVs, we isolated on average approximately 300 tetraspanin-enriched EVs in each region of interest (ROI) while a negligible number was isolated on control, IgG-coated spot, Figure 1f and Table S1. The average localization precision for tetraspanin-enriched EVs was estimated between 7 and 8 nm, Figure S2. We next used TEM data analysis to validate the EV size. We obtained excellent agreement for rEV sizes determined using SMLM imaging followed by Voronoi tessellation analysis (SMLM<sub>T</sub>); SMLM imaging followed by EVSCAN analysis (SMLM<sub>E</sub>, a modified version of DBSCAN, see **Methods** for details), and TEM with segmentation analysis. As expected, nanoparticle tracking analysis (NTA) resulted in slightly larger EV sizes (Figure 1g, Table S1). We also evaluated the shape of rEVs. In particular, circularity or roundness describes

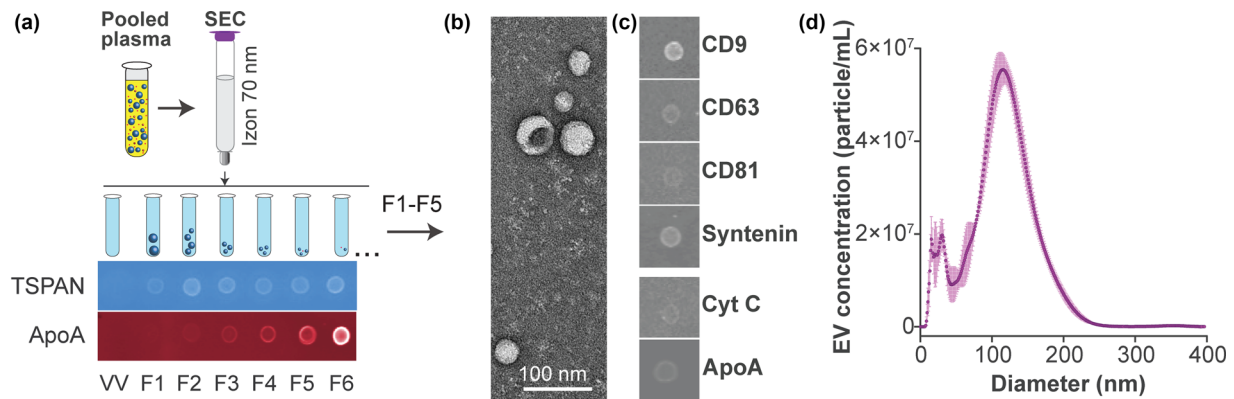


**FIGURE 2** Overview of the isolation and characterization of EVs from pooled human plasma. (a) EVs from the pooled human plasma were enriched using Izon Legacy 70 nm SEC columns; collected fractions were assessed by dot blots. Tetraspanins (TSPAN) CD9, CD63, and CD81 served as positive markers, and ApoA as a confounding protein co-isolated with EVs (Figure S3 contains additional dot blots). Fractions F1-F5 were selected for downstream applications. (b) TEM image of the combined fractions F1-F5 indicates intact EV morphology. (c) Dot blots of the combined fractions F1-F5, assessing the CD9, CD63, CD81 and syntenin content (EV markers); as well as the cytochrome C and ApoA content. (d) Size distribution of the combined fractions F1-F5 acquired using NTA (mean  $\pm$  SEM,  $n = 3$ ). The EV concentration was  $5.17 \times 10^9 \pm 5 \times 10^7$  particle/mL and the average diameter was 120 nm.

how closely a shape of an object approaches that of a perfect circle (1 indicates a perfect circle and 0 represents an increasingly elongated polygon). Excellent agreement was obtained between SMLM and TEM for the circularity measurements (Figure 1h, Table S1).

After validation of the method, we evaluated EVs from pooled human plasma. Isolation of EVs using size exclusion chromatography (SEC) is fast and has high recovery, good purity and good reproducibility (Böing et al., 2014; Kowal et al., 2016; Stranska et al., 2018). Thus, we used Izon 70 nm Legacy columns to enrich for EVs from pooled human plasma (scheme in Figure 2a, top). We assessed fractions for total protein content (Figure S3a). We also evaluated EV markers (CD9, CD63, CD81, syntenin), confounding protein co-isolated with EVs (ApoA) and cytoplasmic marker typically not associated with EVs (cytochrome C) (Jong et al., 2017), Figure S3b and Figure 2a, bottom. Based on this data, we selected fractions F1-F5 that had high EV content and relatively good purity; we combined them for downstream applications. For these SEC-enriched EVs, in line with Minimal Information for Studies of Extracellular Vesicles (MISEV) guidelines (Thery et al., 2018), transmission electron microscopy (TEM, Figure 2b) was used to confirm the intact EV morphology. Dot blots (Figure 2c) were used to confirm the presence of canonical EV markers (tetraspanins CD9, CD63, CD81 and luminal EV protein syntenin) and low expression of ApoA and cytochrome C. NTA (Figure 2d) was used to assess EV concentration and size range.

As with rEVs, we used unlabelled anti-TSPAN Abs to affinity isolate SEC-enriched EVs from pooled human plasma. To outline the EV surface well, we used staining with a combination of three Abs against abundant tetraspanins (CD9, CD63 and CD81) labelled with the same fluorescent dye, AF647. Since the distribution of tetraspanins can be heterogeneous and some EVs may have distinct tetraspanin domains (McNamara et al., 2022), we first assessed the overlap between staining of EV membrane (covalent labelling of available cysteines on EV membranes with CF568-maleimide (Lennon et al., 2022), in yellow, Figure 3a, left) and staining of tetraspanins on EV membrane (affinity labelling of CD9, CD63 and CD81 using AF647-labelled anti-TSPAN Abs, in red, Figure 3a, left). For 632 colocalized EVs, centroid shifts (640 channel relative to 561 channel) are shown in Figure 3a, right. Gaussian distribution of centroid shifts is seen in both x- and y-direction, indicating excellent overlap for the majority of EVs (e.g., EV shown in Figure 3a, left bottom). On average, we observed 24.8 nm centroid shift (with SEM of 0.8 nm), consistent with heterogeneous distribution/clustering of tetraspanins in some EVs (e.g., EV shown in Figure 3a, left top).

We next tested how the number of detected tetraspanin-enriched EVs (isolation and labelling scheme, Figure 1a) in each imaged ROI correlated with sample concentration. We found a significant positive correlation ( $R^2 = 0.9986$ ) in the 64-fold dilution range (Figure 3b). Density was optimal for 1:4 diluted EVs (Figure 3b inset) and average localization precision was estimated at approximately 7 nm (Figure S2); images at all dilutions had excellent signal-to-noise ratio. Next, for 1:4 diluted EVs (Figure 3c and Table S1), we counted the number of detected CD9-, CD63- and CD81-enriched EVs. For these experiments, EVs were isolated on surfaces coated with Abs against only one type of tetraspanin (either CD9, CD63 or CD81) and stained with AF647-labelled anti-TSPAN Abs. In agreement with dot blots (Figure 2c), we obtained the highest yield for CD9-enriched EVs. High levels of CD9-enriched EVs were consistent with a recent report (Karimi et al., 2022) indicating a high number of CD9-positive EVs in EDTA plasma that was used in our study. Raw SMLM images in Figure 3d show clearly defined EVs. We detected a negligible number of EVs with four important controls (Figure 3c, right): (1) EVs were incubated onto coverslips coated with anti-rabbit IgG; (2) EVs were incubated onto coverslips coated with anti-cytochrome C Ab; (3) EVs were lysed with 0.3% Triton X-100 and incubated onto coverslips coated with anti-TSPAN Abs; (4) EVs were incubated on coverslips coated with the polymer

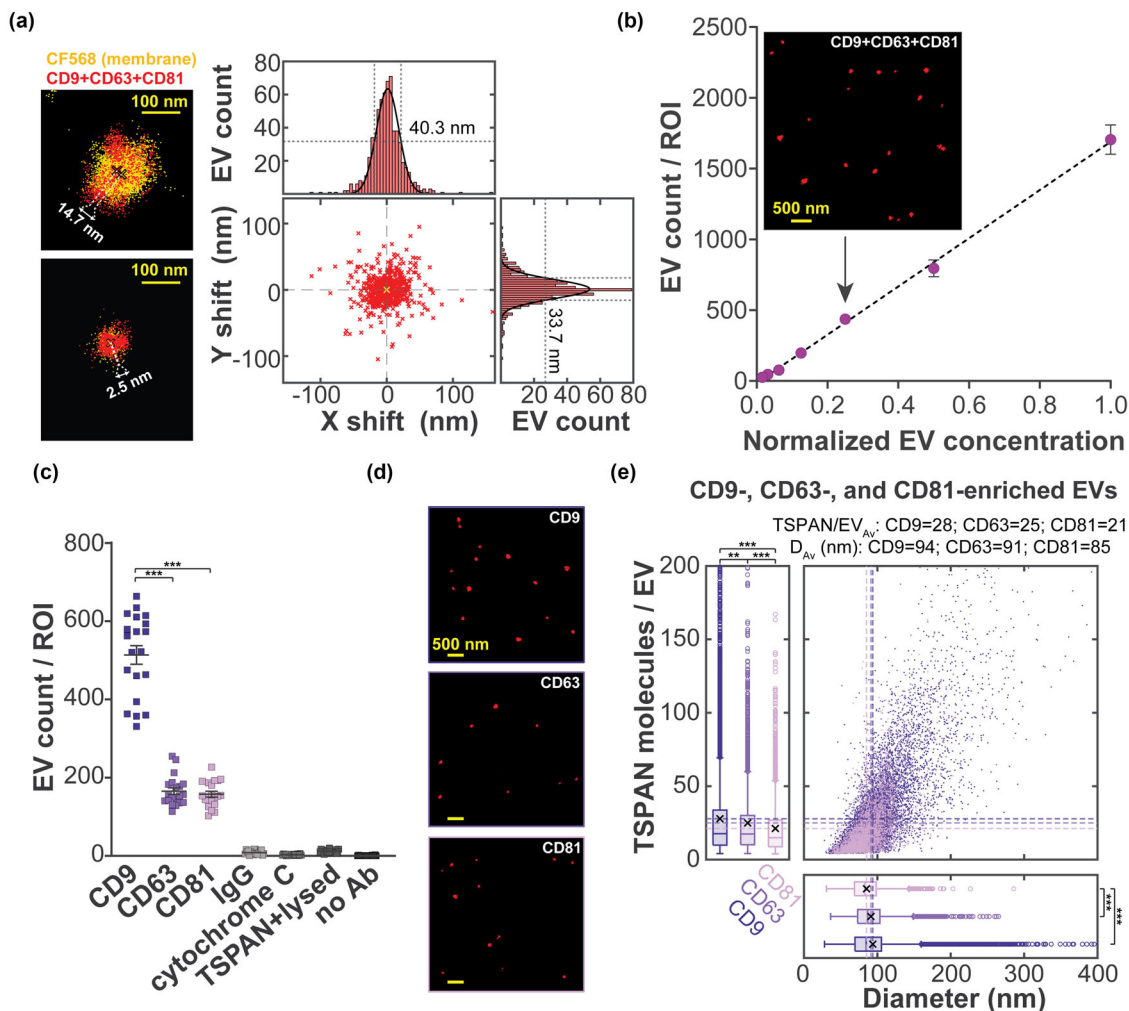


**FIGURE 3** SEVEN for characterization of SEC-enriched EVs from pooled human plasma. (a) Left, Tetraspanin-enriched EVs were detected using CF568-maleimide (labels available cysteine residues on the membrane, yellow) and AF647-labelled anti-TSPAN Abs (labels membrane tetraspanins, red). Right, 2D distribution of relative centroid shifts for two-colour EVs (centroid of the yellow channel is assigned 0,0 position). Full width at half maximum values for Gaussian fittings of EV counts are shown;  $n = 3$ . (b) Number of detected TSPAN-enriched EVs per ROI. The x-axis represents EV concentrations normalized to the highest applied EV concentration (undiluted SEC-enriched EVs). Mean  $\pm$  SEM; minimum  $n = 4$ , 20 ROIs;  $R^2 = 0.9986$ . Inset, Raw SMLM image of TSPAN-enriched EVs. The arrow represents the dilution at which the SMLM image was acquired. (c) Number of detected EVs per ROI in the CD9-, CD63- and CD81-enriched EV subpopulations and controls: anti-rabbit IgG and anti-cytochrome C Abs were immobilized onto surfaces; anti-TSPAN Abs were immobilized onto surfaces and EVs were lysed with Triton X-100; surfaces were not immobilized with Abs. Mean  $\pm$  SEM;  $n = 4$ , 20 ROIs. (d) Raw SMLM images of CD9-, CD63- and CD81-enriched EVs. (e) 2D histograms and corresponding box plots for CD9-, CD63- and CD81-enriched EVs. Each dot represents a single EV with a corresponding diameter (x-axis) and the number of detected TSPAN molecules (y-axis). Box plots: interquartile range (box), median (centre line), mean (cross); the hollow dots indicate EVs detected beyond 1.5-times the interquartile range (marked by the Whisker lines under and over the box).  $n = 4$ , 20 ROIs. \*\* Indicates  $p < 0.01$ ; \*\*\* indicates  $p < 0.001$ . Numerical values and  $p$ -values are provided in Tables S1 and S2.

that was capped (non-fouling surface, no Ab was attached). Figure S4 shows raw SMLM images for these control surfaces. For all controls, we detected only a few EVs. To comprehensively characterize individual EVs, we calculated the diameter and the number of detected TSPAN molecules per EV. In Figure 3e, we show 2D histograms for CD9-, CD63- and CD81-enriched subpopulations obtained for four independent repeats. Each dot represents a detected vesicle and provides its diameter (x-axis) and the number of detected TSPAN molecules (y-axis). For three subpopulations, we calculated mean (cross), median (centre line), interquartile range (box) and coefficient of variation (CV) for size and number of detected TSPAN molecules;  $p$ -values are shown in Table S2. On average (Figure 3e and Table S1), the EV diameter ranged from 85 nm for CD81-enriched EVs to 94 nm for CD9-enriched EVs; the number of detected TSPAN molecules per EV ranged from 21 for CD81-enriched EVs to 28 for CD9-enriched EVs. According to CV values (Table S1), CD81-enriched EVs had the smallest while CD9-enriched EVs had the largest heterogeneity in size and TSPAN content.

While most EVs are round-shaped, there is some morphological heterogeneity (Arraud et al., 2014; Yuana et al., 2013; Zabeo et al., 2017), especially in EVs derived from cancer cells (Ryuzaki et al., 2021). Thus, we also assessed the shape of EVs by calculating



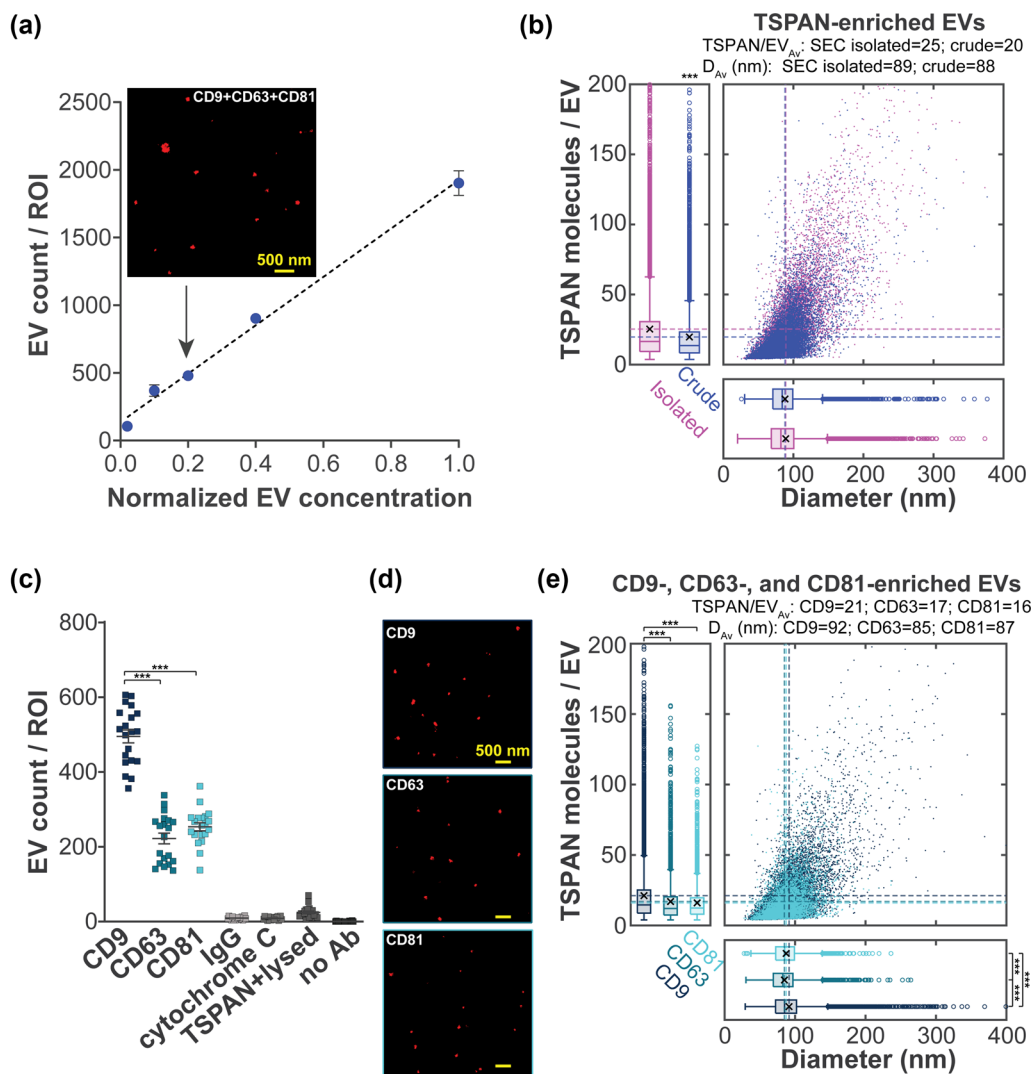


**FIGURE 4** SEVEN for characterization of EVs from crude pooled human plasma. (a) Number of detected TSPAN-enriched EVs per ROI. The x-axis represents EV concentrations normalized to the highest applied EV concentration (1:20 dilution of crude plasma). Mean  $\pm$  SEM;  $n = 3, 15$  ROIs;  $R^2 = 0.9947$ . Inset, Raw SMLM image of TSPAN-enriched EVs. The arrow represents the dilution at which the SMLM image was acquired. (b) 2D histograms and corresponding box plots for TSPAN-enriched EVs from either SEC-enriched or crude plasma samples. Each dot represents a single EV with a corresponding diameter (x-axis) and the number of detected TSPAN molecules (y-axis).  $n = 5, 25$  ROIs. (c) Number of detected EVs per ROI in the CD9-, CD63- and CD81-enriched EV subpopulations and controls: anti-rabbit IgG and anti-cytochrome C Abs were immobilized onto surfaces; anti-TSPAN Abs were immobilized onto surfaces and EVs were lysed with Triton X-100; surfaces were not immobilized with Abs. Mean  $\pm$  SEM;  $n = 4, 20$  ROIs. (d) Raw SMLM images of CD9-, CD63- and CD81-enriched EVs. (e) 2D histograms and corresponding box plots for CD9-, CD63- and CD81-enriched EVs isolated directly from crude plasma. Each dot represents a single EV with a corresponding diameter (x-axis) and the number of detected TSPAN molecules (y-axis).  $n = 4, 20$  ROIs. Box plots in (b, e): interquartile range (box), median (center line), mean (cross); the hollow dots indicate EVs detected beyond 1.5-times the interquartile range (marked by the Whisker lines under and over the box). \*\*\* Indicates  $p < 0.001$ . Numerical values and  $p$ -values are provided in Tables S1–S3.

the circularity in EV subpopulations. As expected, (Figure S5a and Table S1), for all subpopulations EVs were largely round-shaped with circularity values between 0.86 and 0.87.

We extended the SEVEN assay to assess EVs directly from crude plasma (no SEC enrichment). We first investigated tetraspanin-enriched EVs: EVs were isolated on surfaces coated with unlabelled anti-TSPAN Abs and stained with AF647-labelled anti-TSPAN Abs (scheme in Figure 1a). A clear border between the spot coated with anti-TSPAN Abs and passivated coverslip surface is seen, Figure S6a. A high signal-to-noise ratio in SMLM with well-defined EVs was also observed (Figure S6b and inset in Figure 4a); an excellent localization precision, on average 7–8 nm (Figure S2) was estimated. According to data in Figure 4a, the number of detected tetraspanin-enriched EVs per ROI positively correlated with sample concentration in 50-fold dilution range with  $R^2 = 0.9947$ . Importantly, we could detect tetraspanin-enriched EVs from as little as 0.08  $\mu$ L of plasma. This demonstrates the high sensitivity of our assay.

We next compared the characteristics of tetraspanin-enriched EVs between SEC-enriched and crude plasma samples (Figure 4b and Table S3). When normalized to sample volume, we obtained about 4.1-fold more EVs directly from crude plasma. While there was no significant difference in EV size and similar values for circularities were observed (Figures 4b, S5C and Table S3), EVs from crude plasma contained fewer detected TSPAN molecules. This may be due to steric occlusion in EVs from crude plasma. Another way we assessed tetraspanin-enriched EVs from crude plasma was isolation on lactadherin-coated surfaces (lactadherin binds to phospholipids that are present on EV membranes (Yang et al., 2018)) followed by staining with AF647-labelled anti-TSPAN Abs, Figure S7. Of note, fewer EVs were isolated on lactadherin-coated surfaces (compared to anti-TSPAN Abs-coated surfaces, Table S3). Lactadherin may pull down other lipid-containing particles present in the plasma; while these particles would not be visualized in SMLM (they do not contain abundant tetraspanins), they would occupy the surface and limit available binding sites. Importantly, the characteristics of EVs isolated on either anti-TSPAN Abs- or lactadherin-coated surfaces were similar: average values for diameter (88 nm vs. 87 nm), circularity (0.86 vs. 0.85), and detected tetraspanin content per EV (20 vs. 18).

Subpopulation of EVs enriched in specific tetraspanin (EVs were isolated on coverslips coated with one of the three Abs: anti-CD9, anti-CD63 or anti-CD81) and stained with AF647-labelled anti-TSPAN Abs were assessed. For 1:100 plasma dilution, a similar distribution of subpopulations was obtained between SEC-enriched EVs (Figure 3c and Table S1) and crude plasma EVs (Figure 4c and Table S1). Importantly, all controls (EVs were incubated onto coverslips coated with anti-rabbit IgG or anti-cytochrome C Ab, Triton X-100-lysed EVs were incubated onto coverslips coated with anti-TSPAN Abs, or no Ab) resulted in a low number of detected EVs, Figure 4c, right and Figure S8. Moreover, raw SMLM images of EV subpopulations (Figure 4d) indicate that CD9-, CD63- and CD81-enriched EVs were well-defined. For CD9-, CD63- and CD81-enriched EV populations, we robustly defined EV size and detected molecular TSPAN content with corresponding heterogeneities. On average, CD63- and CD81-enriched EVs had similar diameters (85 and 87 nm, respectively) and numbers of detected TSPAN molecules per EV (17 and 16, respectively); CD9-enriched EVs had the largest diameter (92 nm), number of detected TSPAN molecules per EV (21) and heterogeneity in size and TSPAN content (Figure 4e and Table S1). CD9-, CD63- and CD81-enriched EVs had only small differences in average circularities (Figure S5b and Table S1), and most were round-shaped.

We used the ExoView assay (Daaboul et al., 2011, 2016) as a complimentary and commercially available affinity-based approach to assess CD9-, CD63- and CD81-enriched EVs from crude pooled human plasma. This approach provides the size of EVs using single particle interferometry and it determines the presence of proteins of interest on individual EVs based on staining with fluorescent Abs. Fluorescence images of CD81-enriched EVs in three colours (Figure S9a) show individual EVs that express three different tetraspanin markers (CD9 in blue, CD81 in green and CD63 in red). The abundance of CD9-, CD63- and CD81-enriched subpopulations (fluorescence channel) and controls are shown in Figure S10a-e, and Table S4. Additionally, in the fluorescence channel, we evaluated CD41a/CD9 double-positive EVs that may be associated with platelets (Karimi et al., 2022). While these EVs were present as expected (Karimi et al., 2022) based on EDTA-plasma sample origin (Figure S10f and Table S4), their number was lower compared to CD81-enriched subpopulations (CD81-positive EVs are not associated with platelets (Koliha et al., 2016; Sung et al., 2019; Tomlinson, 2009)). We next compared fraction of EVs isolated on control surfaces and capturing efficiency (normalized to sample volume and detection area) for SEVEN and ExoView assays; an excellent agreement was observed (Table S4, bottom). Finally, we evaluated the size of CD9-, CD63- and CD81-enriched EVs from pooled human plasma, Figure S10g and Table S5. Compared to SEVEN, ExoView detected a smaller average size for all three subpopulations, consistent with its more limited size range (50-200 nm) and interferometric EV detection.

We further extended this assay to assess EVs enriched in membrane proteins highly expressed in PDAC. In this pilot study, we assessed four patients with resectable PDAC (patient characteristics are shown in Table S6); their plasma was obtained prior to surgery in EDTA tubes and processed in the same manner (Methods). We first evaluated EVs using ExoView. Images of CD81-enriched EVs that contained tetraspanin markers are shown in Figure S9b; the number of detected EVs (for different subpopulations) in the fluorescence channel is shown in Figure S10a-f. As with pooled healthy plasma, we detected CD41a/CD9 double-positive EVs (indicative of platelet origin) but for each patient, this population was less abundant compared to CD81-enriched EVs (not associated with platelets). Of note, compared to other patients, patient 3 had more CD81-enriched EVs (and also more CD41a/CD9 double-positive EVs). Next, we enriched for EVs from PDAC patient plasma using SEC and evaluated combined fraction F1-F5 with TEM and microfluidic resistive pulse sensing (MRPS). We observed EVs with intact morphology (Figure S11a). The average EV diameter obtained with MRPS (Figure S11b) ranged between 67 and 72 nm for PDAC patients and it was 70 nm for pooled healthy plasma (in all cases, EVs were filtered through 200 nm membrane filter before measurements). EV sizes were also evaluated using ExoView (Figure S11c). The diameter of CD9-enriched EVs ranged between 58 and 59 nm for PDAC patients and it was 60 nm for pooled healthy plasma. Finally, we evaluated patient samples (directly from crude plasma) using SEVEN.

CD9 is highly expressed in PDAC microenvironment (stroma) and its abundance is associated with poor prognosis in PDAC patients (Nigri et al., 2022). Thus, we investigated if we could detect differences in CD9-enriched populations in 1:100 diluted healthy pooled plasma versus 1:100 diluted PDAC plasma samples. While the detected number of CD9-enriched EVs varied between all subjects, CD9-enriched EVs from PDAC patients had on average significantly smaller diameter (91 nm for healthy pooled plasma and 81-86 nm for PDAC patients, Figure 5a and Table S7). Little difference was observed in EV circularity

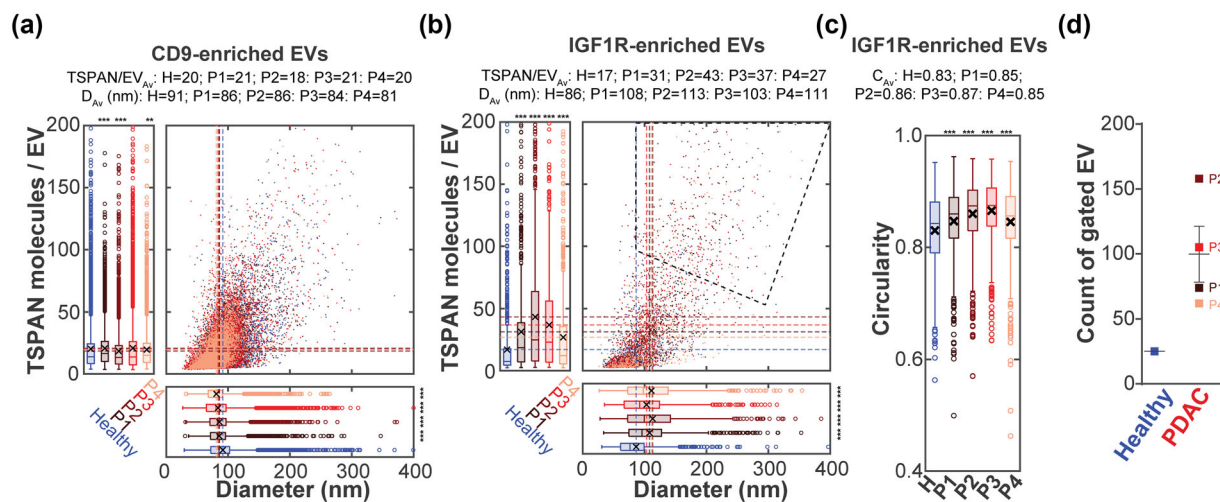


**FIGURE 5** SEVEN for characterization of EVs from PDAC patient plasma. 2D histograms and corresponding box plots for CD9-enriched EVs (a) and IGF1R-enriched EVs (b) isolated from healthy control plasma (blue) and PDAC patient plasma (red colour palette, P1-P4). Each dot represents a single EV with a corresponding diameter (x-axis) and the number of detected TSPAN molecules (y-axis).  $n = 3$ , 15 ROIs. (c) Box plots indicating circularities of IGF1R-enriched EVs isolated from healthy control plasma (blue) and PDAC patient plasma (red colour palette, P1-P4). (d) For IGF1R-enriched EVs, we identified a unique population (indicated by the dashed grey gating polygon in (d)) with a larger diameter and higher TSPAN content. The number of gated EVs for healthy control and PDAC patients is shown. Box plots in (a-c): interquartile range (box), median (centre line), mean (cross); the hollow dots indicate EVs detected beyond 1.5-times the interquartile range (marked by the Whisker lines under and over the box).  $n = 3$ , 15 ROIs. Significance tests were performed against healthy control. \*\* Indicates  $p < 0.01$ ; \*\*\* indicates  $p < 0.001$ . Numerical values and  $p$ -values are provided in Tables S7 and S8.

(Figure S5d, Table S8). Raw SMLM images of CD9-enriched EVs are shown in Figure S12, top. Given that higher expression of IGF1R is associated with worse patient outcomes in resected PDAC (Du et al., 2020), we next assessed IGF1R-enriched EVs. For these experiments, we used a larger volume and higher concentration of diluted plasma (Supplemental Methods) as IGF1R-enriched EVs (compared to tetraspanin-enriched EVs) are significantly less abundant. For healthy pooled plasma, ~0.5% of EVs were IGF1R-enriched. Compared to EVs from healthy pooled plasma, PDAC patients had on average larger IGF1R-enriched EVs (86 nm for healthy pooled plasma and 103–113 nm for PDAC patients) with more detected tetraspanin molecules (Figure 5b and Table S7) and a more rounded shape (Figure 5c and Table S7). Raw SMLM images of IGF1R-enriched EVs are shown in Figure S12, bottom. Based on EV size and molecular tetraspanin content, we gated IGF1R-enriched EVs (polygon, Figure 5b) and found a unique population (Figure 5c) where EVs from PDAC patients were more abundant.

## 4 | DISCUSSION

Here we describe a new assay termed Single Extracellular Vesicle Nanoscopy (SEVEN). SEVEN simultaneously provide a highly sensitive assessment of EV numbers, size, molecular content and shape with their heterogeneities. Our approach was validated using rEVs, described by Geurickx et al. (Geurickx et al., 2019) in their studies on developing new biological reference materials. The rise of EV research aimed at advancing biological understanding, improving diagnostics, and developing therapy requires the corresponding standardized methods to isolate and characterize individual EVs from different biological sources. Two features make rEVs (Geurickx et al., 2019) an excellent reference material for our studies (Figure 1): (1) tetraspanins within these EVs, namely CD9, CD63 and CD81, can be used for affinity pulldown onto coverslips; (2) in commercially obtained reference material (from Millipore Sigma), a fraction of rEVs is eGFP positive. Our analyses of rEVs yielded an excellent overlay between the TIRF image (green, detecting eGFP) and SMLM image (red, detecting tetraspanins). A comparison between SEVEN and TEM demonstrated excellent agreement in both the size and shape of EVs. While both Voronoi tessellation and EVSCAN can be successfully used for SMLM data analysis, we employed the former approach for the rest of the data analysis as codes are available (Andronov et al., 2016) and can be easily user modified. As expected (Bachurski et al., 2019), NTA provided slightly larger values for average EV sizes.

SEVEN was next used to assess EVs from more complex biological samples. We first assessed the distribution of CD9, CD63 and CD81 on tetraspanin-enriched EVs from pooled human plasma (these EVs were first SEC-enriched, Figure 2). We detected EV membrane (CF568-maleimide dye covalently attaches to exposed cysteine residues on EV membrane, providing excellent coverage of EV membrane (Lennon et al., 2022), in yellow) and tetraspanins on the EV membrane (AF647-labelled anti-TSPAN Abs affinity attach to CD9, CD63 and CD81, in red), Figure 3a, left. Most EVs show an excellent overlap between two channels, with the Gaussian distribution of centroid shifts in both x- and y-direction (Figure 3a, right). An average distance of  $24.8 \pm 0.8$  nm

was observed between centroids in the two channels with full width at half maximum (FWHM) values of 40.3 and 33.7 nm in x- and y-direction, respectively. While technical details (e.g., slightly higher noise in the 561 channel) could lead to small centroid shifts, it is likely that EVs with more significant centroid shifts have heterogeneous distribution/clustering of tetraspanins. Although we detect smaller shifts on average, this result would be consistent with a recent report by McNamara et al. (McNamara et al., 2022) pointing to distinct tetraspanin domains on EVs.

We next comprehensively assessed tetraspanin-enriched EVs as well as CD9-, CD63- and CD81-enriched EV subpopulations (Figure 3) in terms of size, shape and detected molecular tetraspanin content. Of note, since here we use fluorescent Abs to detect tetraspanins on EVs attached to surfaces, it is possible that certain tetraspanin sites were not accessible. Images had an outstanding signal-to-noise ratio and average localization precision of approximately 7 nm. Additionally, the assay had a high linearity range (64-fold dilution) with few EVs detected on control surfaces. These important features can provide a robust and precise assessment of individual EVs even from low abundant or low volume samples. This is essential for the assessment of both disease-enriched and organ-enriched EVs.

Importantly, SEVEN allowed us to assess EV subpopulations directly from plasma samples (Figure 4). The approach quantified tetraspanin-enriched EVs from as little as 0.08  $\mu$ L of plasma; the assay was linear in a 50-fold dilution range. There was an excellent agreement in the abundance of EV subpopulations between SEC-enriched and crude plasma samples. SEVEN also demonstrated how SEC enrichment affects EV populations. Tetraspanin-enriched EVs from crude plasma were more abundant. This increase is expected as the loss of EVs during isolation procedures typically occurs. Interestingly, we detected fewer tetraspanin molecules on EVs isolated from crude plasma (Figure 4b). In EVs from crude plasma, some tetraspanin sites may be sterically blocked and SEC may be removing a fraction of EV-associated plasma factors. For example, a recent report suggests that soft corona proteins and/or protein aggregates (Tóth et al., 2021; Wolf et al., 2022) may be removed from EVs using SEC. Regardless of the source of the difference, the result demonstrates that SEVEN may be sensitive to characterizing EV changes associated with isolation.

We used a complementary approach, ExoView assay (Daaboul et al., 2011, 2016), to assess EVs (Figures S9 and S10). The EV capturing efficiency agreed well between SEVEN and ExoView (Table S4). Of note, SEVEN can accurately determine EV size (Figure 1) with excellent localization precision (on average estimated between 7 and 8 nm) and allows for measurement of a broader EV size range (30–400 nm for SEVEN vs. 50–200 nm for ExoView). SEVEN achieved excellent reproducibility between measurements (five operators performed experiments to ensure robustness) with the low signal on control surfaces. Combination of (1) surface chemistry that resulted in minimal background signal and yielded an excellent non-fouling surface with (2) molecular sensitivity and nanoscale precision of SMLM, provided additional, unique capabilities. In particular, we could assess EV shape, quantify the detected molecular content of EVs, and sensitively evaluate low-abundant EVs. These important properties provide unique information that can help differentiate disease-enriched or organ-enriched subpopulations towards biomarker application.

Given the sensitivity of the approach, we used SEVEN to assess EVs from patients with resectable PDAC. PDAC is one of the deadliest tumours (Rahib et al., 2014; Saad et al., 2018); only 10–20% of patients are diagnosed in time to receive potentially curative surgery. Carbohydrate antigen CA19-9 is the only FDA-approved biomarker for diagnosis and post-surgery monitoring of PDAC (Goonetilleke & Siriwardena, 2007). Nevertheless, sensitivity is poor for small early-stage tumours (DiMagno et al., 1999; Goggins, 2005), and the test is ineffective for 10% of the population who have a Lewis-negative phenotype (they do not produce detectable amounts of CA19-9) (Lamerz, 1999; Scarà et al., 2015). New early detection strategies are urgently needed to complement clinical measurements. Thus, we extended SEVEN to assess patients with resectable PDAC (one of the patients was CA19-9 non-expressor, Table S6). We obtained plasma samples prior to surgery, and assessed EVs for size, morphology and marker expression (Figures S9b, S10a-f, S11). Using SEVEN, we evaluated both CD9-enriched and IGF1R-enriched EVs (given their high expression in PDAC (Du et al., 2020; Nigri et al., 2022)). Compared to healthy control (Figures 5 and S12), PDAC patients had (1) smaller CD9-enriched EVs; (2) larger and rounder IGF1R-enriched EVs with more tetraspanin molecules. Interestingly, recent data (Badovinac et al., 2021) indicates that PDAC patients with poorly differentiated resectable tumours had significantly larger plasma EVs. This suggests that the biogenesis or clearance of these EV populations may be affected. Importantly, a unique pancreatic cancer-enriched EV subpopulation may be present (Figure 5d).

Based on excellent sensitivity and precision, SMLM is becoming an increasingly used approach to characterize EVs. Because SEVEN has an affordable coverslip design (~\$10 of consumables per sample) and robust protocol, this approach offers some significant benefits to general EV research as well as studies aimed at advancing our biological understanding of human health and disease. Moreover, SEVEN can be easily customized to assess different subpopulations of EVs using affinity reagents that can be covalently attached to the surface of coverslips. While we used SEVEN to assess EVs from pooled human plasma, the assay can be extended to other biofluids and cultured cells. Additionally, the assay can be extended to multicolour imaging and to detect other cargo molecules (beyond tetraspanins). The flexibility of the approach may be particularly useful for assessing cargo biomarkers. For example, we have previously shown that cardiac troponin T can be sensitively detected using SMLM; cardiac troponin T-positive EVs could provide important information on patient health status complementary to clinical measurements (Lennon et al., 2022). Thus, our work demonstrates that SMLM can sensitively profile both disease-associated and organ-associated EVs in unprecedented detail. When applied to the diagnostic arena, SEVEN has the potential to subphenotype known diseases and outperform conventional biomarkers in the detection of early-stage diseases.



## AUTHOR CONTRIBUTIONS

Conceptualization: Andras Saftics, Gagandeep Singh, Saumya Das, Kendall Van Keuren-Jensen, Tijana Jovanovic-Talisan; Data Acquisition: Andras Saftics, Sarah Abuelreich, Eugenia Romano, Ima Ghaeli, Nan Jiang, Michail Spanos, Kathleen M. Lennon; Data Analysis: Andras Saftics, Sarah Abuelreich, Eugenia Romano, Ima Ghaeli, Nan Jiang, Michail Spanos, Kathleen M. Lennon; Funding Acquisition: Gagandeep Singh, Kendall Van Keuren-Jensen, Saumya Das, Tijana Jovanovic-Talisan; Project Administration: Gagandeep Singh, Saumya Das, Kendall Van Keuren-Jensen, Tijana Jovanovic-Talisan; Manuscript Writing: Andras Saftics, Sarah Abuelreich, Eugenia Romano, Ima Ghaeli, Kathleen M. Lennon, Nan Jiang, Michail Spanos, Gagandeep Singh, Kendall Van Keuren-Jensen, Saumya Das, Tijana Jovanovic-Talisan.

## ACKNOWLEDGEMENTS

Dr. Marcella Chiari for helpful discussions, Dr. John C. Williams for ganitumab, Dr. Ian J. Talisman for manuscript editing, Dr. Alexander Spark and Dr. Alexandre Kitching for help with Nanometrix data analysis. National Institutes of Health grant UG3/UH3 TR002878 (S.D., K.V.K.J., T.J.T.); Dorrance Family Research Fund (K.V.K.J., T.J.T.); Board of Governors of the City of Hope (G.S., T.J.T.), Southwest Food Industries Circle (G.S., T.J.T.), Circle 1500 (T.J.T.), Dancing with Chicago Celebrities (T.J.T.), Bruce & Lyn Everette (G.S., T.J.T.), Irell and Manella Graduate School of Biological Sciences at City of Hope (S.A.). Research reported in this publication included work performed in the City of Hope Analytical Cytometry core supported by the National Cancer Institute of the National Institutes of Health under grant number P30CA033572. The content is solely the responsibility of the authors and does not necessarily represent the official views of the National Institutes of Health.

## CONFLICT OF INTEREST STATEMENT

K.V.J. is a member of the Scientific Advisory Board for HTG and Dyrnamix, neither of which have played a role in this study. S.D. is a founding member and holds equity in Thryv Therapeutics and Switch Therapeutics, and has consulted for Renovacor, none of which played any role in this study. This work is the subject of a provisional patent application. The authors may be entitled to certain compensations through their institutions' respective intellectual property policies in the event such intellectual property is licensed.

## DATA AVAILABILITY STATEMENT

Data generated or analysed during this study are included in this published article and its Supporting Information file. All codes are provided in the references; any modifications are noted in the **Methods** section.

## ORCID

Andras Saftics  <https://orcid.org/0000-0001-7129-6142>

## REFERENCES

- Al-Sukhni, W., Borgida, A., Rothenmund, H., Holter, S., Semotiuk, K., Grant, R., Wilson, S., Moore, M., Narod, S., Jhaveri, K., Haider, M. A., & Gallinger, S. (2012). Screening for pancreatic cancer in a high-risk cohort: An eight-year experience. *Journal of Gastrointestinal Surgery: Official Journal of the Society for Surgery of the Alimentary Tract*, 16, 771–783. <https://doi.org/10.1007/s11605-011-1781-6>
- Andronov, L., Orlov, I., Lutz, Y., Vonesch, J. L., & Klahlolz, B. P. (2016). ClusterViSu, a method for clustering of protein complexes by Voronoi tessellation in super-resolution microscopy. *Scientific Reports*, 6, 24084. <https://doi.org/10.1038/srep24084>
- Annibale, P., Vanni, S., Scarselli, M., Rothlisberger, U., & Radenovic, A. (2011). Quantitative photo activated localization microscopy: Unraveling the effects of photoblinking. *PLoS One*, 6, e22678. <https://doi.org/10.1371/journal.pone.0022678>
- Arraud, N., Linares, R., Tan, S., Gounou, C., Pasquet, J. M., Mornet, S., & Brisson, A. R. (2014). Extracellular vesicles from blood plasma: Determination of their morphology, size, phenotype and concentration. *Journal of Thrombosis and Haemostasis: JTH*, 12, 614–627. <https://doi.org/10.1111/jth.12554>
- Bachurski, D., Schuldner, M., Nguyen, P. H., Malz, A., Reiners, K. S., Grenzi, P. C., Babatz, F., Schauss, A. C., Hansen, H. P., Hallek, M., & Pogge von Strandmann, E. (2019). Extracellular vesicle measurements with nanoparticle tracking analysis - An accuracy and repeatability comparison between NanoSight NS300 and ZetaView. *Journal of Extracellular Vesicles*, 8, 1596016. <https://doi.org/10.1080/20013078.2019.1596016>
- Badovinac, D., Goričar, K., Zavrtnik, H., Petrič, M., Lavrin, T., Mavec, N., Dolžan, V., Tomažič, A., & Lenassi, M. (2021). Plasma extracellular vesicle characteristics correlate with tumor differentiation and predict overall survival in patients with pancreatic ductal adenocarcinoma undergoing surgery with curative intent. *Journal of Personalized Medicine*, 11, 77. <https://doi.org/10.3390/jpm11020077>
- Bei, Y., Das, S., Rodosthenous, R. S., Holvoet, P., Vanhaverbeke, M., Monteiro, M. C., Monteiro, V. V. S., Radosinska, J., Bartekova, M., Jansen, F., Li, Q., Rajasingh, J., & Xiao, J. (2017). Extracellular vesicles in cardiovascular theranostics. *Theranostics*, 7, 4168–4182. <https://doi.org/10.7150/thno.21274>
- Böing, A. N., van der Pol, E., Grootemaat, A. E., Coumans, F. A., Sturk, A., & Nieuwland, R. (2014). Single-step isolation of extracellular vesicles by size-exclusion chromatography. *Journal of Extracellular Vesicles*, 3, 23430. <https://doi.org/10.3402/jev.v3.23430>
- Cherbonneau, F., Li, G., Gokulnath, P., Sahu, P., Prunevieville, A., Kitchen, R., Benichou, G., Larghero, J., Domian, I., & Das, S. (2022). TRACE-seq: A transgenic system for unbiased and non-invasive transcriptome profiling of living cells. *iScience*, 25, 103806. <https://doi.org/10.1016/j.isci.2022.103806>
- Colombo, M., Raposo, G., & Théry, C. (2014). Biogenesis, secretion, and intercellular interactions of exosomes and other extracellular vesicles. *Annual Review of Cell and Developmental Biology*, 30, 255–289. <https://doi.org/10.1146/annurev-cellbio-101512-122326>
- Conroy, T., Desseigne, F., Ychou, M., Bouché, O., Guimbaud, R., Bécauarn, Y., Adenis, A., Raoul, J. L., Gourgou-Bourgade, S., de la Fouchardière, C., Bennouna, J., Bachet, J. B., Khemissa-Akouz, F., Péré-Vergé, D., Delbaldo, C., Assenat, E., Chauffert, B., Michel, P., Montoto-Grillot, C., ... Groupe Tumeurs Digestives of Unicancer, PRODIGE Intergroup. (2011). FOLFIRINOX versus gemcitabine for metastatic pancreatic cancer. *The New England Journal of Medicine*, 364, 1817–1825. <https://doi.org/10.1056/NEJMoa1011923>

- Daaboul, G. G., Gagni, P., Benussi, L., Bettotti, P., Ciani, M., Cretich, M., Freedman, D. S., Ghidoni, R., Ozkumur, A. Y., Piotto, C., Prosperi, D., Santini, B., Ünlü, M. S., & Chiari, M. (2016). Digital detection of exosomes by interferometric imaging. *Scientific Reports*, 6, 37246. <https://doi.org/10.1038/srep37246>
- Daaboul, G. G., Vedula, R. S., Ahn, S., Lopez, C. A., Reddington, A., Ozkumur, E., & Ünlü, M. S. (2011). LED-based interferometric reflectance imaging sensor for quantitative dynamic monitoring of biomolecular interactions. *Biosensors and Bioelectronics*, 26, 2221–2227. <https://doi.org/10.1016/j.bios.2010.09.038>
- Dempsey, G. T., Vaughan, J. C., Chen, K. H., Bates, M., & Zhuang, X. W. (2011). Evaluation of fluorophores for optimal performance in localization-based super-resolution imaging. *Nature Methods*, 8, 1027–1036. <https://doi.org/10.1038/nmeth.1768>
- DiMagno, E. P., Reber, H. A., & Tempero, M. A. (1999). AGA technical review on the epidemiology, diagnosis, and treatment of pancreatic ductal adenocarcinoma. American Gastroenterological Association. *Gastroenterology*, 117, 1464–1484.
- Di Vizio, D., Kim, J., Hager, M. H., Morello, M., Yang, W., Lafargue, C. J., True, L. D., Rubin, M. A., Adam, R. M., Beroukhi, R., Demichelis, F., & Freeman, M. R. (2009). Oncosome formation in prostate cancer: Association with a region of frequent chromosomal deletion in metastatic disease. *Cancer Research*, 69(13), 5601–5609. <https://doi.org/10.1158/0008-5472.Can-08-3860>
- Doyle, L. M., & Wang, M. Z. (2019). Overview of extracellular vesicles, their origin, composition, purpose, and methods for exosome isolation and analysis. *Cells*, 8, 727. <https://doi.org/10.3390/cells8070727>
- Du, C., da Silva, A., Morales-Oyarvide, V., Dias Costa, A., Kozak, M. M., Dunne, R. F., Rubinson, D. A., Perez, K., Masugi, Y., Hamada, T., Brais, L. K., Yuan, C., Babic, A., Ducar, M. D., Thorner, A. R., Aguirre, A., Kulke, M. H., Ng, K., Clancy, T. E., ... Nowak, J. A. (2020). Insulin-like growth factor-1 receptor expression and disease recurrence and survival in patients with resected pancreatic ductal adenocarcinoma. *Cancer Epidemiology, Biomarkers & Prevention: A Publication of the American Association for Cancer Research, Cosponsored by the American Society of Preventive Oncology*, 29, 1586–1595. <https://doi.org/10.1158/1055-9965.Epi-19-1315>
- Endesfelder, U., Malkusch, S., Fricke, F., & Heilemann, M. (2014). A simple method to estimate the average localization precision of a single-molecule localization microscopy experiment. *Histochemistry and Cell Biology*, 141, 629–638. <https://doi.org/10.1007/s00418-014-1192-3>
- Ferguson, S., Yang, K. S., & Weissleder, R. (2022). Single extracellular vesicle analysis for early cancer detection. *Trends in Molecular Medicine*, 28(8), 681–692. <https://doi.org/10.1016/j.molmed.2022.05.003>
- Ferguson, S., Yang, K. S., Zelga, P., Liss, A. S., Carlson, J. C. T., Del Castillo, C. F., & Weissleder, R. (2022). Single-EV analysis (sEVA) of mutated proteins allows detection of stage I pancreatic cancer. *Science Advances*, 8, eabm3453. <https://doi.org/10.1126/sciadv.abm3453>
- Gebara, N., Scheel, J., Skovronova, R., Grange, C., Marozio, L., Gupta, S., Giorgione, V., Caicci, F., Benedetto, C., Khalil, A., & Bussolati, B. (2022). Single extracellular vesicle analysis in human amniotic fluid shows evidence of phenotype alterations in preeclampsia. *Journal of Extracellular Vesicles*, 11, e12217.
- Geurickx, E., Tulkens, J., Dhondt, B., Van Deun, J., Lippens, L., Vergauwen, G., Heyman, E., De Sutter, D., Gevaert, K., Impens, F., Miinalainen, I., Van Bockstal, P. J., De Beer, T., Wauben, M. H. M., Nolte-’t-Hoen, E. N. M., Bloch, K., Swinnen, J. V., van der Pol, E., Nieuwland, R., ... Hendrix, A. (2019). The generation and use of recombinant extracellular vesicles as biological reference material. *Nature Communications*, 10, 3288. <https://doi.org/10.1038/s41467-019-11182-0>
- Goggins, M. (2005). Molecular markers of early pancreatic cancer. *Journal of Clinical Oncology: Official Journal of the American Society of Clinical Oncology*, 23, 4524–4531. <https://doi.org/10.1200/jco.2005.19.711>
- Golfetto, O., Wakefield, D. L., Cacao, E. E., Avery, K. N., Kenyon, V., Jorand, R., Tobin, S. J., Biswas, S., Gutierrez, J., Clinton, R., Ma, Y., Horne, D. A., Williams, J. C., & Jovanović-Talisman, T. (2018). A platform to enhance quantitative single molecule localization microscopy. *Journal of the American Chemical Society*, 140, 12785–12797. <https://doi.org/10.1021/jacs.8b04939>
- Goonetilleke, K. S., & Siriwardena, A. K. (2007). Systematic review of carbohydrate antigen (CA 19-9) as a biochemical marker in the diagnosis of pancreatic cancer. *European Journal of Surgical Oncology: The Journal of the European Society of Surgical Oncology and the British Association of Surgical Oncology*, 33, 266–270. <https://doi.org/10.1016/j.ejso.2006.10.004>
- Jong, A. Y., Wu, C. H., Li, J., Sun, J., Fabbri, M., Wayne, A. S., & Seeger, R. C. (2017). Large-scale isolation and cytotoxicity of extracellular vesicles derived from activated human natural killer cells. *Journal of Extracellular Vesicles*, 6, 1294368. <https://doi.org/10.1080/20013078.2017.1294368>
- Karimi, N., Dalirfardouei, R., Dias, T., Lötvall, J., & Lässer, C. (2022). Tetraspanins distinguish separate extracellular vesicle subpopulations in human serum and plasma - Contributions of platelet extracellular vesicles in plasma samples. *Journal of Extracellular Vesicles*, 11, e12213. <https://doi.org/10.1002/jev2.12213>
- Khater, I. M., Nabi, I. R., & Hamarneh, G. (2020). A review of super-resolution single-molecule localization microscopy cluster analysis and quantification methods. *Patterns (N Y)*, 1, 100038. <https://doi.org/10.1016/j.patter.2020.100038>
- Kim, E. R., Bae, S. Y., Lee, K. H., Lee, K. T., Son, H. J., Rhee, J. C., & Lee, J. K. (2011). Is health screening beneficial for early detection and prognostic improvement in pancreatic cancer? *Gut and Liver*, 5, 194–199. <https://doi.org/10.5009/gnl.2011.5.2.194>
- King, H. W., Michael, M. Z., & Gleadle, J. M. (2012). Hypoxic enhancement of exosome release by breast cancer cells. *BMC Cancer*, 12, 421. <https://doi.org/10.1186/1471-2407-12-421>
- Koliha, N., Wienczek, Y., Heider, U., Jüngst, C., Kladt, N., Krauthäuser, S., Johnston, I. C., Bosio, A., Schauss, A., & Wild, S. (2016). A novel multiplex bead-based platform highlights the diversity of extracellular vesicles. *Journal of Extracellular Vesicles*, 5, 29975. <https://doi.org/10.3402/jev.v5.29975>
- Kotrbová, A., Štěpka, K., Maška, M., Páleník, J. J., Ilkovic, L., Klemová, D., Kravec, M., Hubatka, F., Dave, Z., Hampl, A., Bryja, V., Matula, P., & Pospíchalová, V. (2019). TEM ExosomeAnalyzer: A computer-assisted software tool for quantitative evaluation of extracellular vesicles in transmission electron microscopy images. *Journal of Extracellular Vesicles*, 8, 1560808. <https://doi.org/10.1080/20013078.2018.1560808>
- Kowal, J., Arras, G., Colombo, M., Jouve, M., Morath, J. P., Primdal-Bengtson, B., Dingli, F., Loew, D., Tkach, M., & Théry, C. (2016). Proteomic comparison defines novel markers to characterize heterogeneous populations of extracellular vesicle subtypes. *Proceedings of the National Academy of Sciences of the United States of America*, 113, E968–977. <https://doi.org/10.1073/pnas.1521230113>
- Lamerz, R. (1999). Role of tumour markers, cytogenetics. *Annals of Oncology*, 10(4), 145–149.
- Lee, S. H., Shin, J. Y., Lee, A., & Bustamante, C. (2012). Counting single photoactivatable fluorescent molecules by photoactivated localization microscopy (PALM). *Proceedings of the National Academy of Sciences of the United States of America*, 109, 17436–17441. <https://doi.org/10.1073/pnas.1215175109>
- Lee, T. H., D’Asti, E., Magnus, N., Al-Nedawi, K., Meehan, B., & Rak, J. (2011). Microvesicles as mediators of intercellular communication in cancer—The emerging science of cellular ‘debris’. *Seminars in Immunopathology*, 33, 455–467. <https://doi.org/10.1007/s00281-011-0250-3>
- Lelek, M., Gyparakis, M. T., Beliu, G., Schueder, F., Griffié, J., Manley, S., Jungmann, R., Sauer, M., Lakadamyali, M., & Zimmer, C. (2021). Single-molecule localization microscopy. *Nature Reviews Methods Primers*, 1, 39. <https://doi.org/10.1038/s43586-021-00038-x>
- Lennon, K. M., Saftics, A., Abuelreich, S., Sahu, P., Lehmann, H. I., Maddox, A. L., Bagabas, R., Januzzi, J. L., Van Keuren-Jensen, K., Shah, R., Das, S., & Jovanovic-Talisman, T. (2022). Cardiac troponin T in extracellular vesicles as a novel biomarker in human cardiovascular disease. *Clinical and Translational Medicine*, 12, e979. <https://doi.org/10.1002/ctm2.979>
- Lennon, K. M., Wakefield, D. L., Maddox, A. L., Brehove, M. S., Willner, A. N., Garcia-Mansfield, K., Meechoovet, B., Reiman, R., Hutchins, E., Miller, M. M., Goel, A., Pirrotte, P., Van Keuren-Jensen, K., & Jovanovic-Talisman, T. (2019). Single molecule characterization of individual extracellular vesicles from pancreatic cancer. *Journal of Extracellular Vesicles*, 8, 1685634–1685634. <https://doi.org/10.1080/20013078.2019.1685634>

- Li, D., Xie, K., Wolff, R., & Abbruzzese, J. L. (2004). Pancreatic cancer. *Lancet*, 363, 1049–1057. [https://doi.org/10.1016/s0140-6736\(04\)15841-8](https://doi.org/10.1016/s0140-6736(04)15841-8)
- Maire, C. L., Fuh, M. M., Kaulich, K., Fita, K. D., Stevic, L., Heiland, D. H., Welsh, J. A., Jones, J. C., Görgens, A., Ricklefs, T., Dührsen, L., Sauvigny, T., Joosse, S. A., Reifenberger, G., Pantel, K., Glatzel, M., Miklosi, A. G., Felce, J. H., Caselli, M., ... Ricklefs, F. L. (2021). Genome-wide methylation profiling of glioblastoma cell-derived extracellular vesicle DNA allows tumor classification. *Neuro-Oncology*, 23, 1087–1099. <https://doi.org/10.1093/neuonc/noab012>
- McNamara, R. P., Zhou, Y., Eason, A. B., Landis, J. T., Chambers, M. G., Willcox, S., Peterson, T. A., Schouest, B., Maness, N. J., MacLean, A. G., Costantini, L. M., Griffith, J. D., & Dittmer, D. P. (2022). Imaging of surface microdomains on individual extracellular vesicles in 3-D. *Journal of Extracellular Vesicles*, 11, e12191. <https://doi.org/10.1002/jev2.12191>
- Mondal, A., Ashiq, K. A., Phulpagar, P., Singh, D. K., & Shiras, A. (2019). Effective visualization and easy tracking of extracellular vesicles in glioma cells. *Biological Procedures Online*, 21, 4. <https://doi.org/10.1186/s12575-019-0092-2>
- Nigri, J., Leca, J., Tubiana, S. S., Finetti, P., Guillaumond, F., Martinez, S., Lac, S., Iovanna, J. L., Audebert, S., Camoin, L., Vasseur, S., Bertucci, F., & Tomasini, R. (2022). CD9 mediates the uptake of extracellular vesicles from cancer-associated fibroblasts that promote pancreatic cancer cell aggressiveness. *Science Signaling*, 15, eabg8191. <https://doi.org/10.1126/scisignal.abg8191>
- Nizamudeen, Z., Markus, R., Lodge, R., Parmenter, C., Platt, M., Chakrabarti, L., & Sottile, V. (2018). Rapid and accurate analysis of stem cell-derived extracellular vesicles with super resolution microscopy and live imaging. *Biochimica et Biophysica Acta. Molecular Cell Research*, 1865, 1891–1900. <https://doi.org/10.1016/j.bbamcr.2018.09.008>
- Oleksiuk, O., Abba, M., Tezcan, K. C., Schaufler, W., Bestvater, F., Patil, N., Birk, U., Hafner, M., Altevogt, P., Cremer, C., & Allgayer, H. (2015). Single-molecule localization microscopy allows for the analysis of cancer metastasis-specific miRNA distribution on the nanoscale. *Oncotarget*, 6, 44745–44757. <https://doi.org/10.18632/oncotarget.6297>
- Rahib, L., Smith, B. D., Aizenberg, R., Rosenzweig, A. B., Fleshman, J. M., & Matrisian, L. M. (2014). Projecting cancer incidence and deaths to 2030: The unexpected burden of thyroid, liver, and pancreas cancers in the United States. *Cancer Research*, 74, 2913–2921. <https://doi.org/10.1158/0008-5472.can-14-0155>
- Ratajczak, J., Wysoczynski, M., Hayek, F., Janowska-Wieczorek, A., & Ratajczak, M. Z. (2006). Membrane-derived microvesicles: Important and underappreciated mediators of cell-to-cell communication. *Leukemia*, 20, 1487–1495. <https://doi.org/10.1038/sj.leu.2404296>
- Ryuzaki, S., Yasui, T., Tsutsui, M., Yokota, K., Komoto, Y., Paisrisarn, P., Kaji, N., Ito, D., Tamada, K., Ochiya, T., Taniguchi, M., Baba, Y., & Kawai, T. (2021). Rapid discrimination of extracellular vesicles by shape distribution analysis. *Analytical Chemistry*, 93, 7037–7044. <https://doi.org/10.1021/acs.analchem.1c00258>
- Saad, A. M., Turk, T., Al-Husseini, M. J., & Abdel-Rahman, O. (2018). Trends in pancreatic adenocarcinoma incidence and mortality in the United States in the last four decades; a SEER-based study. *BMC Cancer*, 18, 688. <https://doi.org/10.1186/s12885-018-4610-4>
- Scarà, S., Bottoni, P., & Scatena, R. (2015). CA 19-9: Biochemical and clinical aspects. *Advances in Experimental Medicine and Biology*, 867, 247–260. [https://doi.org/10.1007/978-94-017-7215-0\\_15](https://doi.org/10.1007/978-94-017-7215-0_15)
- Sharma, S., LeClaire, M., Wohlschlegel, J., & Gimzewski, J. (2020). Impact of isolation methods on the biophysical heterogeneity of single extracellular vesicles. *Scientific Reports*, 10, 13327. <https://doi.org/10.1038/s41598-020-70245-1>
- Silva, A. M., Lázaro-Ibáñez, E., Gunnarsson, A., Dhande, A., Daaboul, G., Peacock, B., Osteikoetxea, X., Salmond, N., Friis, K. P., Shatnyeva, O., & Dekker, N. (2021). Quantification of protein cargo loading into engineered extracellular vesicles at single-vesicle and single-molecule resolution. *Journal of Extracellular Vesicles*, 10, e12130. <https://doi.org/10.1002/jev2.12130>
- Stranska, R., Gysbrechts, L., Wouters, J., Vermeersch, P., Bloch, K., Dierickx, D., Andrei, G., & Snoeck, R. (2018). Comparison of membrane affinity-based method with size-exclusion chromatography for isolation of exosome-like vesicles from human plasma. *Journal of Translational Medicine*, 16, 1. <https://doi.org/10.1186/s12967-017-1374-6>
- Sung, P. S., Huang, T. F., & Hsieh, S. L. (2019). Extracellular vesicles from CLEC2-activated platelets enhance dengue virus-induced lethality via CLEC5A/TLR2. *Nature Communications*, 10, 2402. <https://doi.org/10.1038/s41467-019-10360-4>
- Thery, C., Witwer, K. W., Aikawa, E., Alcaraz, M. J., Anderson, J. D., Andriantsitohaina, R., Antoniou, A., Arab, T., Archer, F., Atkin-Smith, G. K., Ayre, D. C., Bach, J. M., Bachurski, D., Baharvand, H., Balaj, L., Baldacchino, S., Bauer, N. N., Baxter, A. A., Bebawy, M., ... Zuba-Surma, E. K. (2018). Minimal information for studies of extracellular vesicles 2018 (MISEV2018): A position statement of the International Society for Extracellular Vesicles and update of the MISEV2014 guidelines. *Journal of Extracellular Vesicles*, 7, 1535750. <https://doi.org/10.1080/20013078.2018.1535750>
- Tobin, S. J., Wakefield, D. L., Jones, V., Liu, X., Schmolze, D., & Jovanović-Taliman, T. (2018). Single molecule localization microscopy coupled with touch preparation for the quantification of trastuzumab-bound HER2. *Scientific Reports*, 11, 15154.
- Tomlinson, M. G. (2009). Platelet tetraspanins: Small but interesting. *Journal of Thrombosis and Haemostasis: JTH*, 7, 2070–2073. <https://doi.org/10.1111/j.1538-7836.2009.03613.x>
- Tóth, E., Turiák, L., Visnovitz, T., Cserép, C., Mázló, A., Sódar, B. W., Försönits, A. I., Petővári, G., Sebestyén, A., Komlósi, Z., Drahos, L., Kittel, Á., Nagy, G., Bácsi, A., Dénes, Á., Gho, Y. S., Szabó-Taylor, K. É., & Buzás, E. I. (2021). Formation of a protein corona on the surface of extracellular vesicles in blood plasma. *Journal of Extracellular Vesicles*, 10, e12140. <https://doi.org/10.1002/jev2.12140>
- Von Hoff, D. D., Ervin, T., Arena, F. P., Chiorean, E. G., Infante, J., Moore, M., Seay, T., Tjulandin, S. A., Ma, W. W., Saleh, M. N., Harris, M., Reni, M., Dowden, S., Laheru, D., Bahary, N., Ramanathan, R. K., Taberner, J., Hidalgo, M., Goldstein, D., ... Renschler, M. F. (2013). Increased survival in pancreatic cancer with nab-paclitaxel plus gemcitabine. *The New England Journal of Medicine*, 369, 1691–1703. <https://doi.org/10.1056/NEJMoa1304369>
- Willms, E., Cabañas, C., Mäger, I., Wood, M. J. A., & Vader, P. (2018). Extracellular vesicle heterogeneity: Subpopulations, isolation techniques, and diverse functions in cancer progression. *Frontiers in Immunology*, 9, 738. <https://doi.org/10.3389/fimmu.2018.00738>
- Wolf, M., Poupardin, R. W., Ebner-Peking, P., Andrade, A. C., Blöchl, C., Obermayer, A., Gomes, F. G., Vari, B., Maeding, N., Eminger, E., Binder, H. M., Raninger, A. M., Hochmann, S., Bracht, G., Spittler, A., Heuser, T., Ofir, R., Huber, C. G., Aberman, Z., ... Strunk, D. (2022). A functional corona around extracellular vesicles enhances angiogenesis, skin regeneration and immunomodulation. *Journal of Extracellular Vesicles*, 11, e12207. <https://doi.org/10.1002/jev2.12207>
- Yáñez-Mó, M., Siljander, P. R., Andreu, Z., Zavec, A. B., Borrás, F. E., Buzas, E. I., Buzas, K., Casal, E., Cappello, F., Carvalho, J., Colás, E., Cordeiro-da Silva, A., Fais, S., Falcon-Perez, J. M., Ghoobrial, I. M., Giebel, B., Gimona, M., Graner, M., Gursel, I., ... De Wever, O. (2015). Biological properties of extracellular vesicles and their physiological functions. *Journal of Extracellular Vesicles*, 4, 27066. <https://doi.org/10.3402/jev.v4.27066>
- Yang, Y., Hong, Y., Cho, E., Kim, G. B., & Kim, I. S. (2018). Extracellular vesicles as a platform for membrane-associated therapeutic protein delivery. *Journal of Extracellular Vesicles*, 7, 1440131. <https://doi.org/10.1080/20013078.2018.1440131>
- Yuana, Y., Koning, R. I., Kuil, M. E., Rensen, P. C., Koster, A. J., Bertina, R. M., & Osanto, S. (2013). Cryo-electron microscopy of extracellular vesicles in fresh plasma. *Journal of Extracellular Vesicles*, 2, 21494. <https://doi.org/10.3402/jev.v2i0.21494>
- Zabeo, D., Cvjetkovic, A., Lässer, C., Schorb, M., Lötval, J., & Höög, J. L. (2017). Exosomes purified from a single cell type have diverse morphology. *Journal of Extracellular Vesicles*, 6, 1329476. <https://doi.org/10.1080/20013078.2017.1329476>
- Zhu, Y., Zhang, H., Chen, N., Hao, J., Jin, H., & Ma, X. (2020). Diagnostic value of various liquid biopsy methods for pancreatic cancer: A systematic review and meta-analysis. *Medicine (Baltimore)*, 99, e18581. <https://doi.org/10.1097/md.00000000000018581>

Zong, S., Zong, J., Chen, C., Jiang, X., Zhang, Y., Wang, Z., & Cui, Y. (2018). Single molecule localization imaging of exosomes using blinking silicon quantum dots. *Nanotechnology*, 29, 065705. <https://doi.org/10.1088/1361-6528/aaa375>

## SUPPORTING INFORMATION

Additional supporting information can be found online in the Supporting Information section at the end of this article.

**How to cite this article:** Saftics, A., Abuelreich, S., Romano, E., Ghaeli, I., Jiang, N., Spanos, M., Lennon, K. M., Singh, G., Das, S., Van Keuren-Jensen, K., & Jovanovic-Talisman, T. (2023). Single Extracellular Vesicle Nanoscopy. *Journal of Extracellular Vesicles*, 12, e12346. <https://doi.org/10.1002/jev2.12346>